Supplement of Atmos. Chem. Phys., 23, 2365–2378, 2023
https://doi.org/10.5194/acp-23-2365-2023-supplement

Atmospheric Chemistry and Physics
Open Access

Supplement of

The shifting of secondary inorganic aerosol formation mechanisms during haze aggravation: the decisive role of aerosol liquid water

Fei Xie et al.

Correspondence to: Jinyuan Xin (xjy@mail.iap.ac.cn) and Changwei Lü (lcw2008@imu.edu.cn)

Supplement

S1 Data acquisition and analysis methods

S1.1 Data acquisition

On-line ion-chromatograph instrument (MARGA ADI 2080, Metrohm Applikon, Switzerland) was widely used to measure the water-soluble inorganic ions (Na^+, NH_4^+, Mg^{2+}, Ca^{2+}, K^+, Cl^-, F^-, SO_4^{2-}, NO_3^-) in $PM_{2.5}$ and corresponding trace gases (SO_2, HNO_2, HNO_3, HCl, NH_3). In detail, 10 ppm H_2O_2 filled wet rotary denuder (WRD) were used to absorb the gaseous pollutants (e.g., HF, HCl, HNO_3, HONO, SO_2, NH_3), while particulate species (e.g., F^-, Cl^-, NO_3^-, SO_4^{2-}, NH_4^+, Na^+, K^+, Mg^{2+}, Ca^{2+}) were collected by steam jet aerosol collector. By synchronizing occupying atmospheric sampling speed of 16.7L/min and WRD rotation speed of $\geqslant$8rpm, the absorption efficiency of whole instrument reached greater than 99.7%, which makes the samples are reliable. Then, both gaseous and particulate samples are simultaneously transferred as liquid (aqueous) samples and analyzed by ion chromatography. An internal calibration standard containing Li^+ and Br^- with 1h-resolution was simultaneously injected with sample to account for any changes in the system. In addition, external standard solutions were also used to ensure perk identification and data quality. The detection limits of the particulate analytes were 0.001, 0.005, 0.004, 0.005, 0.005, 0.009, 0.006, 0.009 μg/m^3 for Cl^-, NO_3^-, SO_4^{2-}, NH_4^+, Na^+, K^+, Mg^{2+}, Ca^{2+}, respectively. Gaseous analytes detection limits were 0.001, 0.005, 0.002, 0.003, 0.005μg/m^3 for HCl, HNO_3, HNO_2, SO_2, NH_3, respectively.

S1.2 Calculation of HNO_3-NO_3^- partitioning (ε (NO_3^T))

The S curve of HNO_3-NO_3^- partitioning ($\varepsilon(NO_3^-)$) has been adopted and discussed explicitly in many works based on the situ observations. To calculate the theoretical HNO_3-NO_3^-

* Corresponding author, Email: xjy@mail.iap.ac.cn; lcw2008@imu.edu.cn

partitioning and estimate the NO_3^- loadings on particulate matter, theoretical calculation method of HNO_3-NO_3^- partitioning ($\varepsilon(NO_3^T)$) (Guo et al., 2015; Guo et al., 2016; Guo et al., 2017) was employed in this work. Briefly, this calculation was based on equilibrium between HNO_3 and particle-phase NO_3^- (aqueous nitrate concentration). This equilibrium involves two reversible processes, dissolution of HNO_3 into aqueous phase and dissociation of HNO_3 into H^+ and NO_3^-. These two processes are always reach thermodynamic equilibriums at ambient conditions.

$$1st\ HNO_{3(g)} \leftrightarrow HNO_{3(aq)}, H_{HNO_3}$$

$$2nd\ HNO_{3(aq)} \leftrightarrow H^+ + NO_3^-, K_{n1}$$

Thus, according to the definition of Henry's law constant and acid dissociation constant, we have

$$H_{HNO_3} = \gamma_{HNO_3}[HNO_3]/p_{HNO_3}$$

$$K_{n1} = \frac{\gamma_{NO_3^-}[NO_3^-]\gamma_{H^+}[H^+]}{\gamma_{HNO_3}[HNO_3]}$$

thus, based on calculation by Guo et al. (2016), $\varepsilon(NO_3^T)$ could be written as :

$$\varepsilon(NO_3^T) = \frac{H^*_{HNO_3} W_i \times 0.987 \times 10^{-14}}{\gamma_{NO_3^-}\gamma_{H^+}10^{-pH} + H^*_{HNO_3} W_i \times 0.987 \times 10^{-14}}$$

where 0.987 comes from the conversion from 1 atm to 1 bar, Wi is calculated as aerosol liquid water associated with inorganic species in $\mu g/m^3$ (here, aerosol liquid water associated with organics is not considered, due to the extremely low concentrations). R is ideal molar gas constant. T is temperature in K. $H^*_{HNO_3}$ is calculated by the method proposed by Clegg and Brimblecombe (1990).

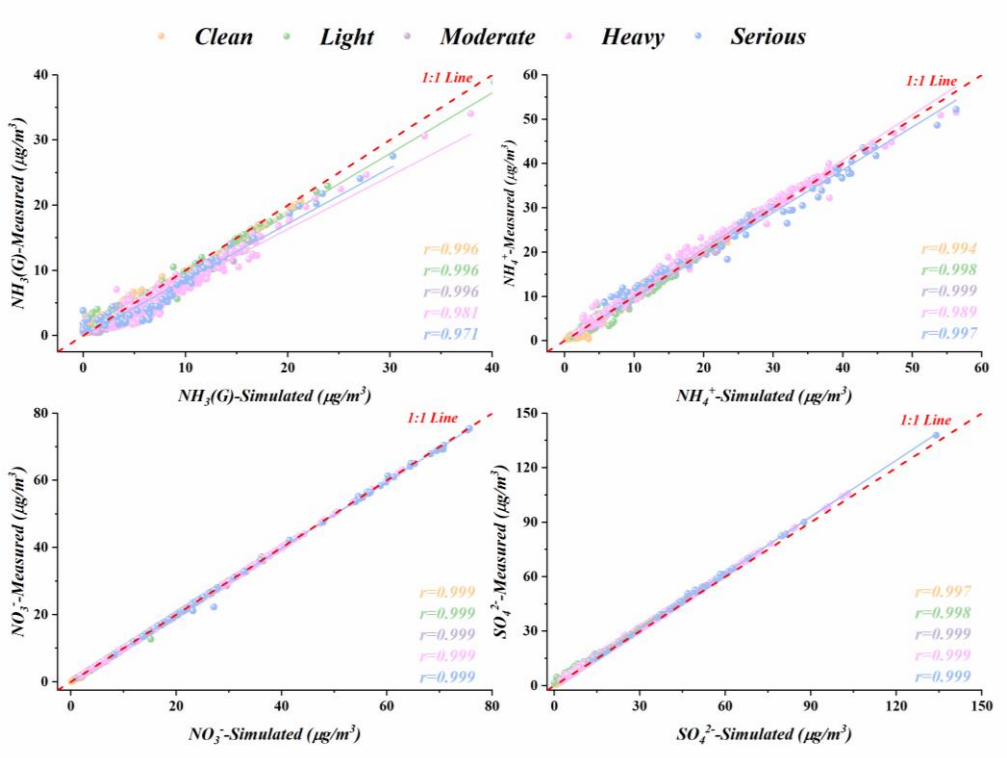

Fig. S1 Correlations of NH_3, NH_4^+, NO_3^- and SO_4^{2-} between measured and ISORROPIA-II simulated results

S2 Results and Discussion

S2.1 In-situ high-resolution observations

The average concentrations of PM_{10}, $PM_{2.5}$, $PM_{1.0}$ were 108.5±68.3, 84.75±84.5, 63.18±96.0 μg/m^3, respectively, with a wide range of variability due to several haze events occurred during the studied period (Fig. S2). It was notable that SO_2 was maintained at a relatively low level (18.97±15.0 μg/m^3) since the implementation of pollution controlling policy in recent years, compared with the neighboring city in 2014 (Zhou et al., 2018) and its own SO_2 concentration during 2014 (50 μg/m^3). Whereas, concentrations of other reactive precursors were basically maintained at relative high level, such as NO_2 (44.56±18.6 μg/m^3), NH_3 (5.55±4.07 μg/m^3), compared with 2014 (Yearly average NO_2 concentration, 44 μg/m^3). Meanwhile, as a typical tracer of combustion, significantly elevated CO emphasized contributions of incomplete combustion on haze intensification. In addition, O_3 was the only significantly declined pollutant with the haze aggravation, due to the weakened solar radiation led by the aggravated haze, which indicating significantly reduces the SIA formation processes through the oxidation between gaseous precursors, OH radicals and stabilized Criegee intermediate (sCI) by

considering the determining role of O_3 in the formation of OH radicals and sCI in the atmosphere (Mauldin Iii et al., 2012; Hua et al., 2008). As for meteorological conditions, low temperature and high humidity were observed during the studied period, with the values were -8.45±4.42 ℃ and 65.59±14.07 %, respectively.

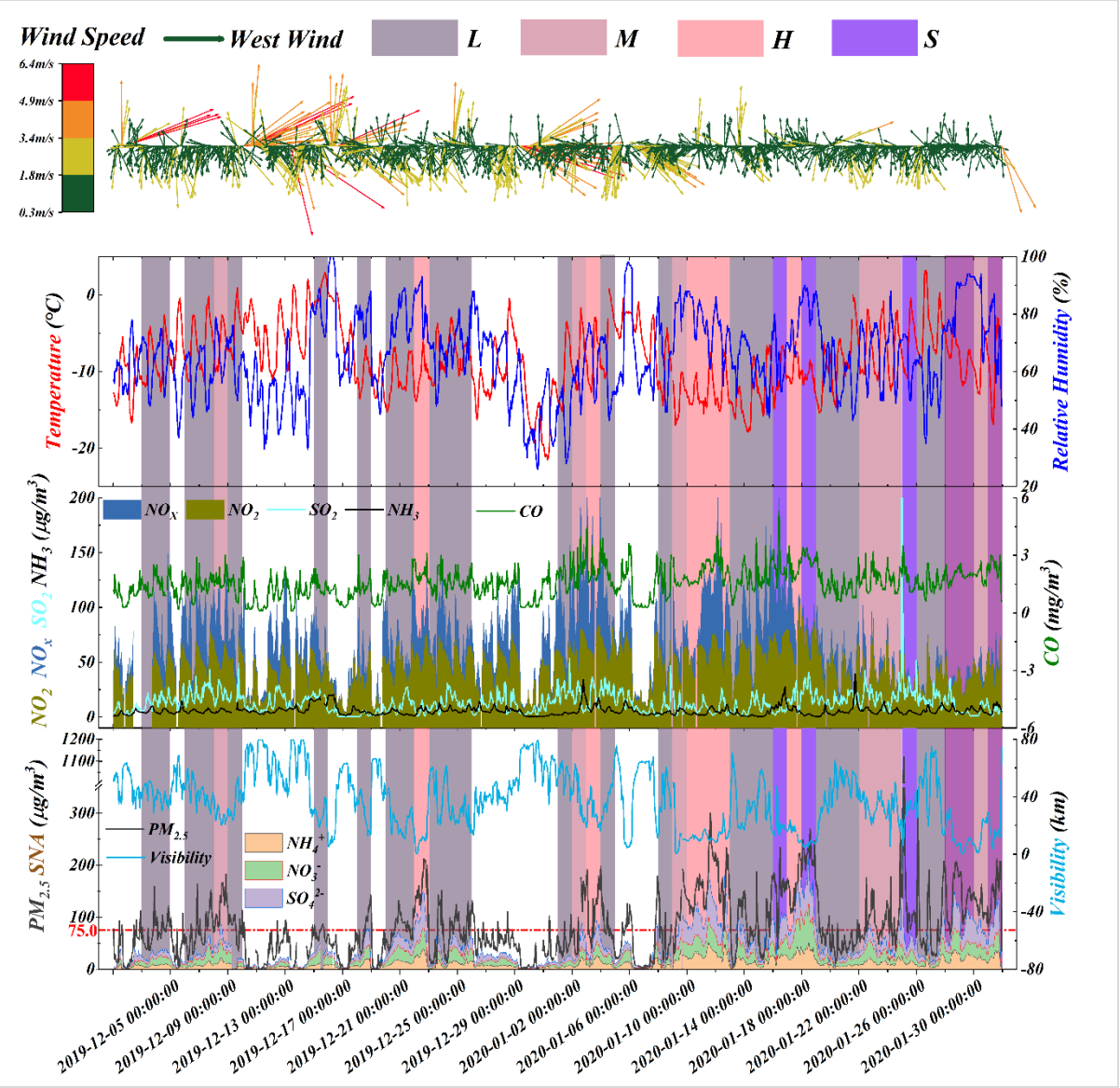

Fig. S2 Time series of meteorological conditions and atmospheric pollutants

$PM_{2.5}$ concentrations presented increasing trends with pollution levels (Fig. S3), and its pH ranged from 0.63 to 6.32 (calculated by ISORROPIA-II), mainly concentrated at 4~5 (Fig. S4). The weak acidic nature of particles was consistent with Tianjin, China (Gao et al., 2020). With the worsening of the haze events, the average concentrations of gaseous precursors, such as SO_2, NO_x, NH_3, were 2.27, 1.33, 1.26 times of those in clean periods, respectively, indicating the increasingly enhanced importance of precursors on SIA generations. Additionally, it was

notable that along with haze aggravation, SIA consecutively sharing the most abundant species in $PM_{2.5}$ and all detected ions, highlighting the determining role of SIA on regional haze aggravation and consistent with previous works (Fig. S3) (Xu et al., 2017; Gao et al., 2020; Huang et al., 2020). Meanwhile, the stabilized conditions, characterized by gradually lower wind speed (from 1.79±1.2 to 1.15±0.47 m/s) and higher RH (from 59.48±15.0 to 71.13±11.9 %) during haze events, further aggravating the regional haze by hindering the diffusion of particulates and accelerating its hygroscopic growth (Tab. S1) (Zhang et al., 2009; Zheng et al., 2015; Zhang et al., 2015).

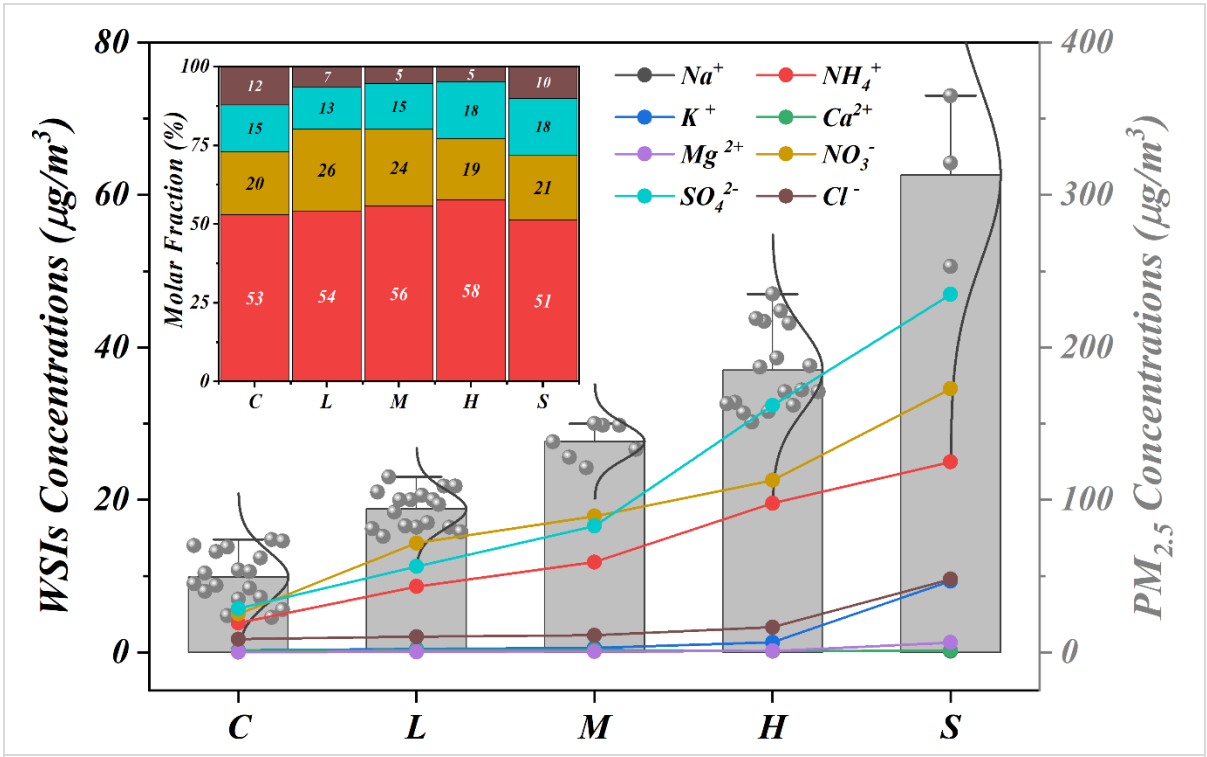

Fig. S3 Characteristics of WSIs under various pollution periods

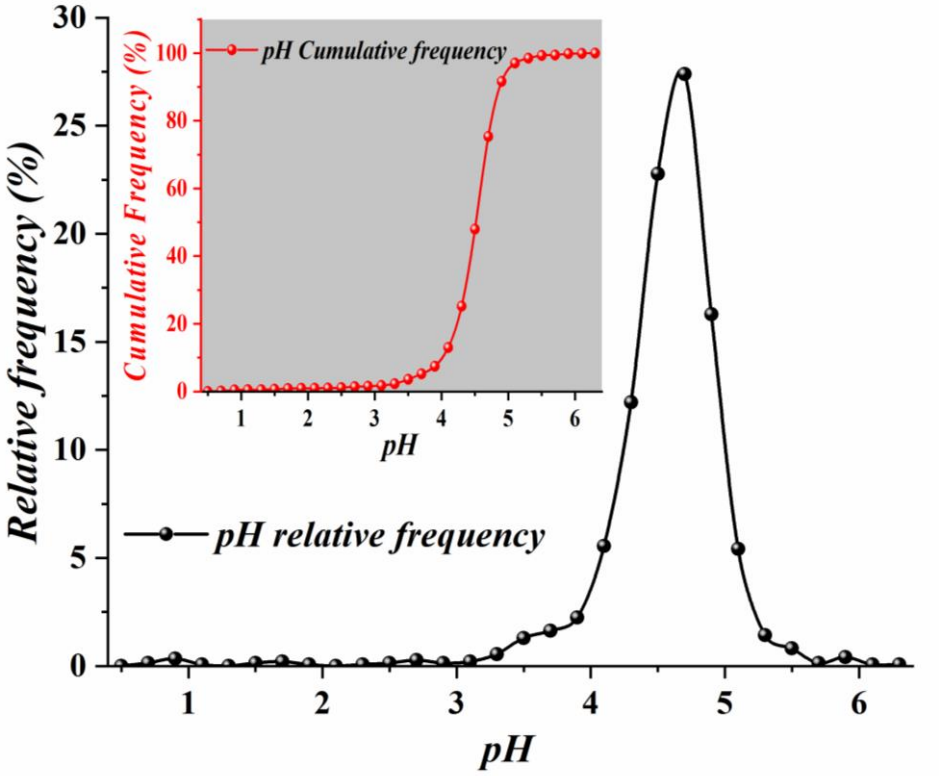

Fig. S4 pH distribution frequency during the studied campaign

S2.2 Chemical forms of ammonium species

Although anions could react with metal ions to form non-volatile compounds, the mass fraction of metal ions (Na^+, K^+, Mg^{2+}, Ca^{2+}) to total ions was less than 5.2% and could be neglected in this work. Thus, molar ratios of NH_4^+ vs. anions could be treated as indicators to identify the chemical forms of ammonium salts guided by stoichiometry (Zhou et al., 2018; Wang et al., 2021; Liu et al., 2017). Briefly, NH_3 prefer react with H_2SO_4 to form non-volatile NH_4HSO_4 or $(NH_4)_2SO_4$ under NH_4^+-poor conditions, afterwards, semi-volatile NH_4NO_3 and NH_4Cl would subsequently generate by existing sufficient NH_3 through neutralize atmospheric HNO_3 and HCl. Roughly, average molar fractions of NH_4^+ accounting for nearly four times of sulfate molar concentrations throughout the studied periods (Fig. S3), indicating the atmospheric SO_4^{2-} were completely neutralized by NH_4^+ and formed ammonium sulfate and ammonia bisulfate according to the stoichiometry results between NH_4^+ and sulfate (Zhou et al., 2018; Wang et al., 2021; Liu et al., 2017). According to Fig. S5a, significant correlations between n (NH_4^+) and n (SO_4^{2-}) with correlation coefficient of 0.947 and slope much lower than 0.5 further highlighting the atmospheric SO_4^{2-} completely neutralized by NH_4^+ to yield ammonium sulfate and ammonia bisulfate. To further deduce the chemical species of the remaining ammonium, the concept of "excess NH_4^+", which calculated as $[NH_4^+]$-1.5×$[SO_4^{2-}]$ in molar concentration

(Shi et al., 2019), was introduced in this work. The correlations between n (excess NH_4^+) and n(NO_3^-) (Fig. S5b) suggested that atmospheric NH_4^+ not only enough to neutralize both SO_4^{2-} and NO_3^- forming two major species of $(NH_4)_2SO_4$ and NH_4NO_3 during any pollution stage, but also remained on particles as free NH_4^+ according to the gas ratio (GR) >1 (Fig. S6). It indicated NH_4NO_3 formation was limited by the availability of HNO_3 (Paulot et al., 2016). Besides, starting with light pollution periods, the scatters of n (excess NH_4^+) and n (Cl^-+NO_3^-) gradually moves from above 1:1 line to below 1:1 line, indicating the coexistence of particle NH_4NO_3 and NH_4Cl and increasingly ammonium ionized on particulate matter from this period (Fig.S5c). Meanwhile, Table S2 showed that the molar concentrations of Cl^- and K^+ significantly elevated from Moderate pollution stage, especially Serious stage, indicating the enhanced emission of biomass burning and coal combustion during these periods. During haze aggravation, the remained-NH_4^+ ([NH_4^+]-1.5×[SO_4^{2-}]-[NO_3^-]) was observed as 0.045, 0.0865, 0.141, 0.281 and 0.316 μmol/m^3 in Clean, Light, Moderate, Heavy and Serious pollution stages, respectively. With the increasing remained-NH_4^+ during haze aggravation, the increasing molar concentrations of Cl^- had more opportunities to meet NH_4^+ and form NH_4Cl, considering the higher molar concentrations of Cl^- than (K^++Na^+). Additionally, the remaining ammonium, as well as other detected alkalic cations, may react with undetected CO_3^{2-}, HCO_3^- and organic materials (e.g., water-soluble organic acids, sugars, alcohols, etc.) through complexation reaction and form metal coordination compounds (Nozière et al., 2010; Chang-Graham et al., 2011; Cui et al., 2021).

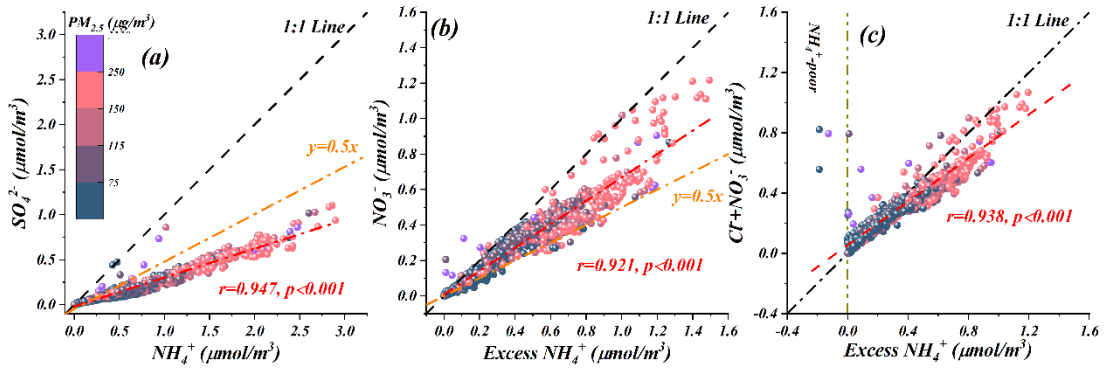

Fig. S5 Correlations between NH_4^+ and water-soluble anions among various pollution periods

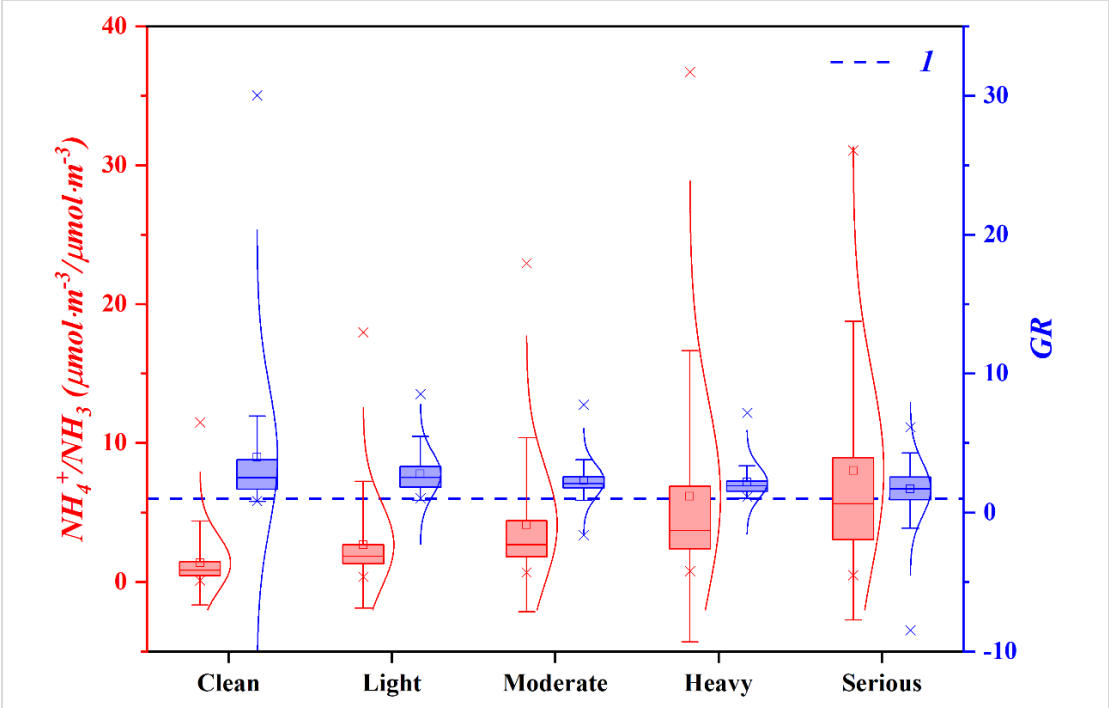

Fig. S6 Box-type of NH_4^+/NH_3 and gas ratio (GR)

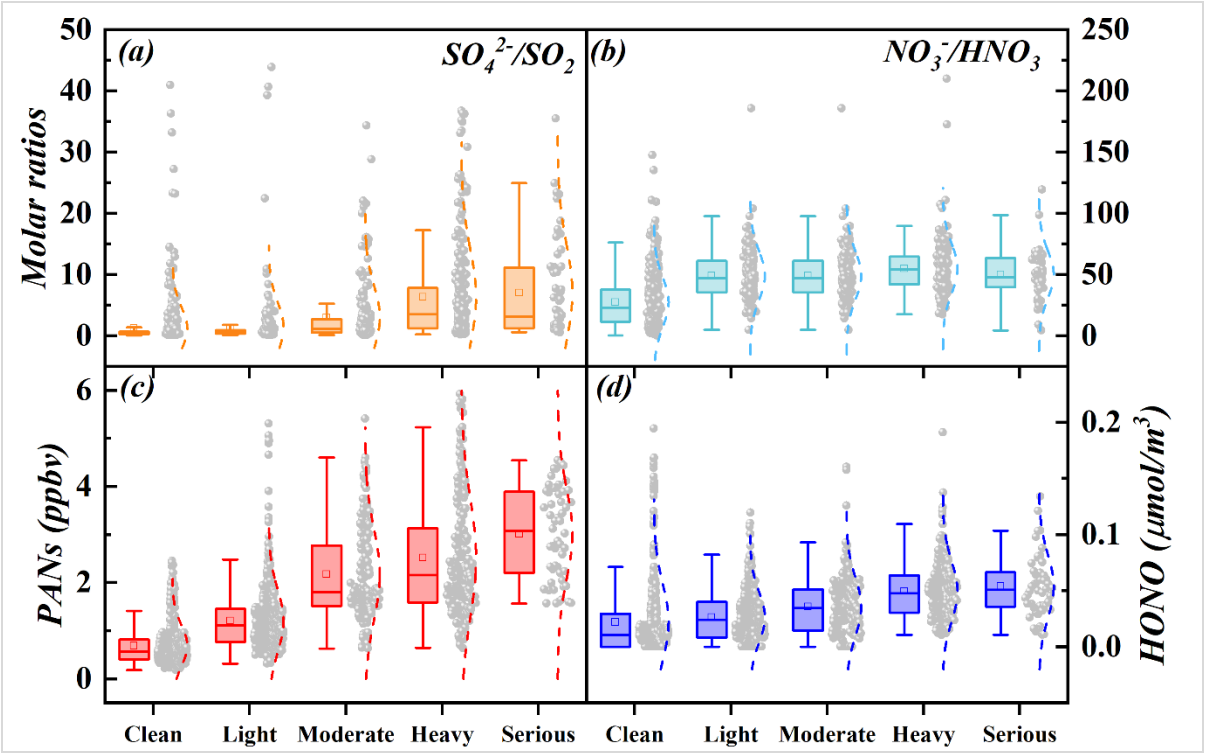

Fig. S7 Box-type of (a) SO_4^{2-}/SO_2, (b)NO_3^-/HNO_3, (c)PANs and (d)HONO response to different pollution stages

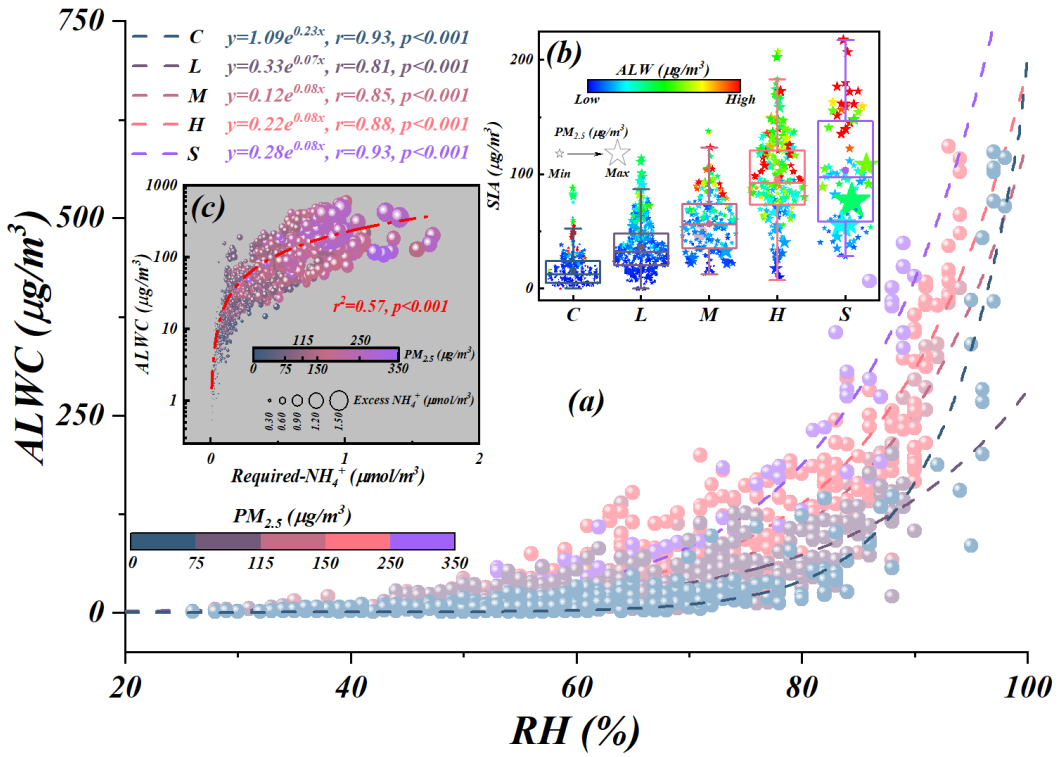

Fig. S8 (a)Correlations of $PM_{2.5}$ concentrations and ALWC with different pollution stages, (b) SIA mass fractions in PM2.5 during entire periods. The pentagrams were colored as a function of aerosol liquid water content, and the size of pentagrams corresponding to the PM2.5 mass concentrations, (c) Correlations between Required- NH_4^+ and ALWC corresponding to $PM_{2.5}$ and excess-NH_4^+, required NH_4^+ and excessNH_4^+ were calculated according to the formula in S.M. text S2

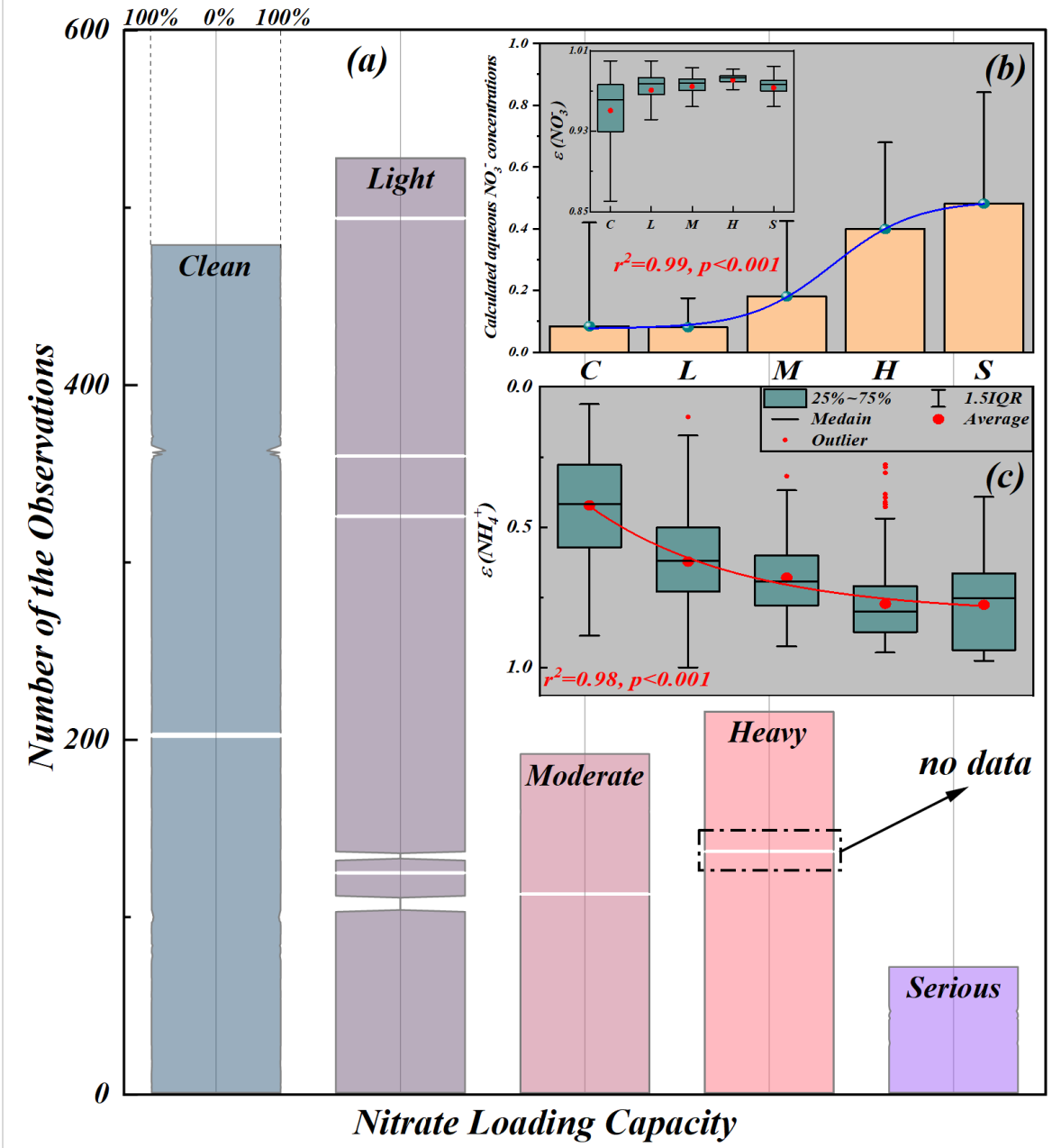

Fig. S9 (a) Statistics of time series of nitrate loading capacity response to different pollution stages, (c) statistics of ε(NH_4^+) response to different pollution stages, (b) calculated aqueous-NO_3^- concentrations and ε(NO_3^-) corresponding to pollution stages, the calculation processes followed by Guo et al. (2015); Guo et al. (2016); Guo et al. (2017)

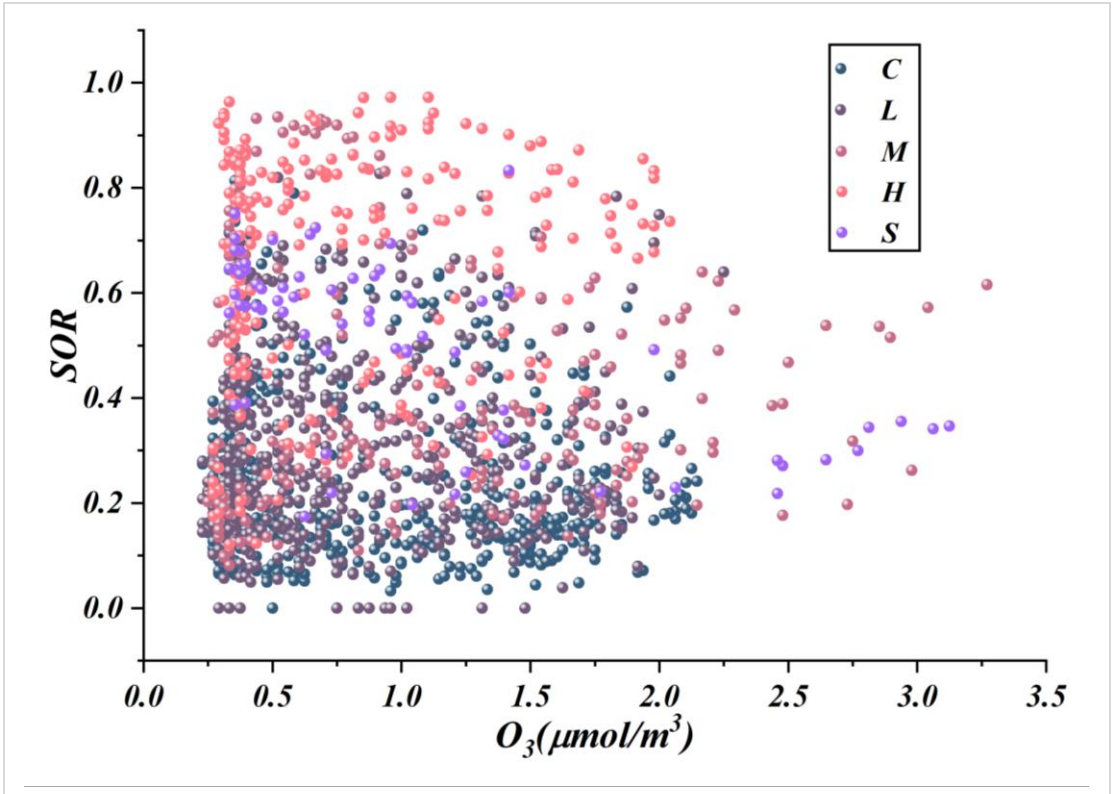

Fig. S10 Correlations between O_3 and SOR response to different pollution stages

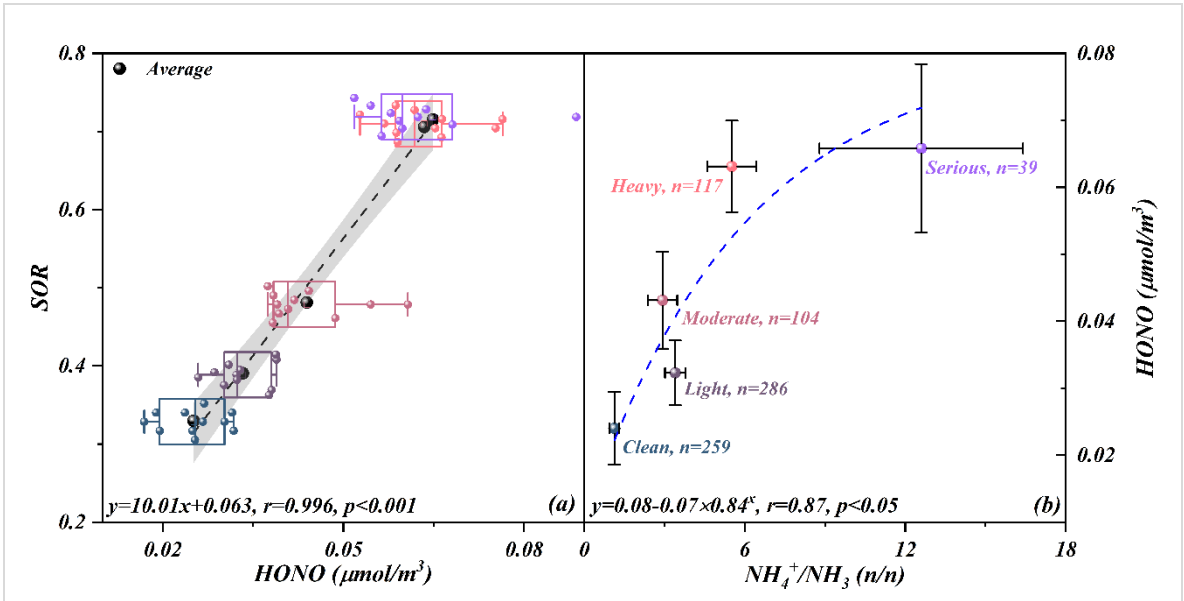

Fig. S11 Correlations between (a) HONO and SOR, (b) NH_4^+/NH_3 and HONO response to different pollution stages. To minimize the dependences mixed layer depth during diurnal changes and avoid the fast photolysis of HONO in the daytime, the nighttime hours were selected and corresponding to 20:00-7:00

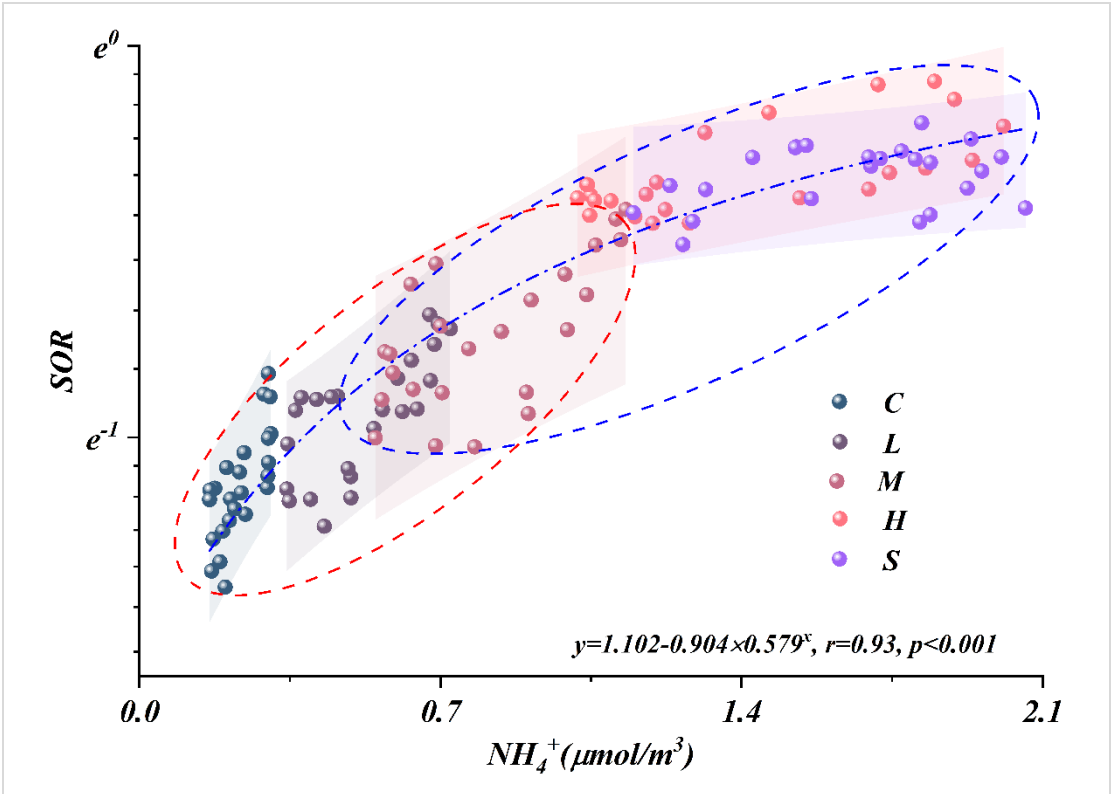

Fig. S12 Correlations between NH_4^+ and SOR response to different pollution stages

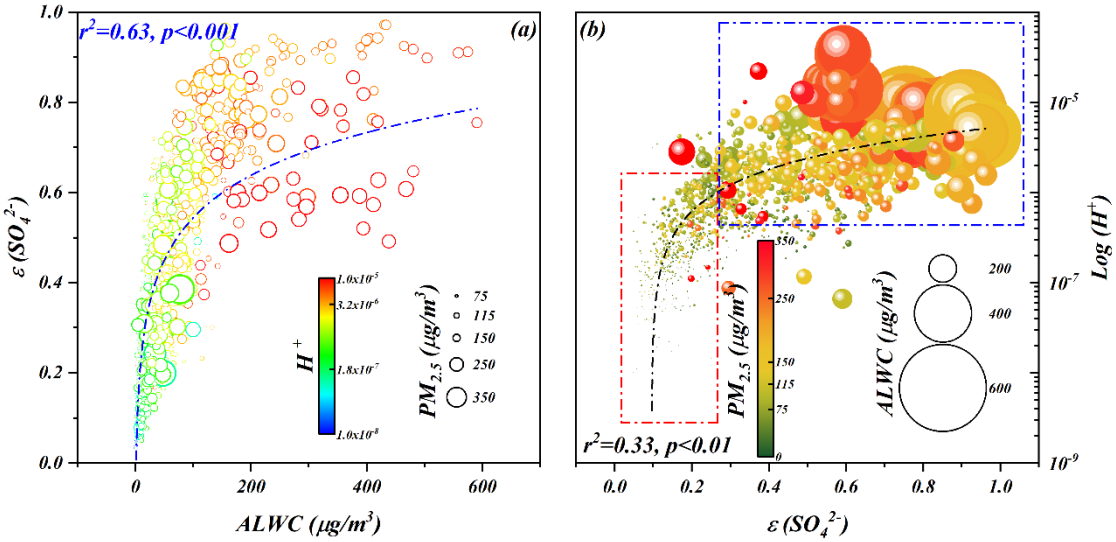

Fig. S13 (a) correlations between ALWC and ε(SO_4^{2-}) corresponding to H^+ and $PM_{2.5}$, (b) correlations betweenε (SO_4^{2-}) and log(H^+) corresponding to $PM_{2.5}$ and ALWC

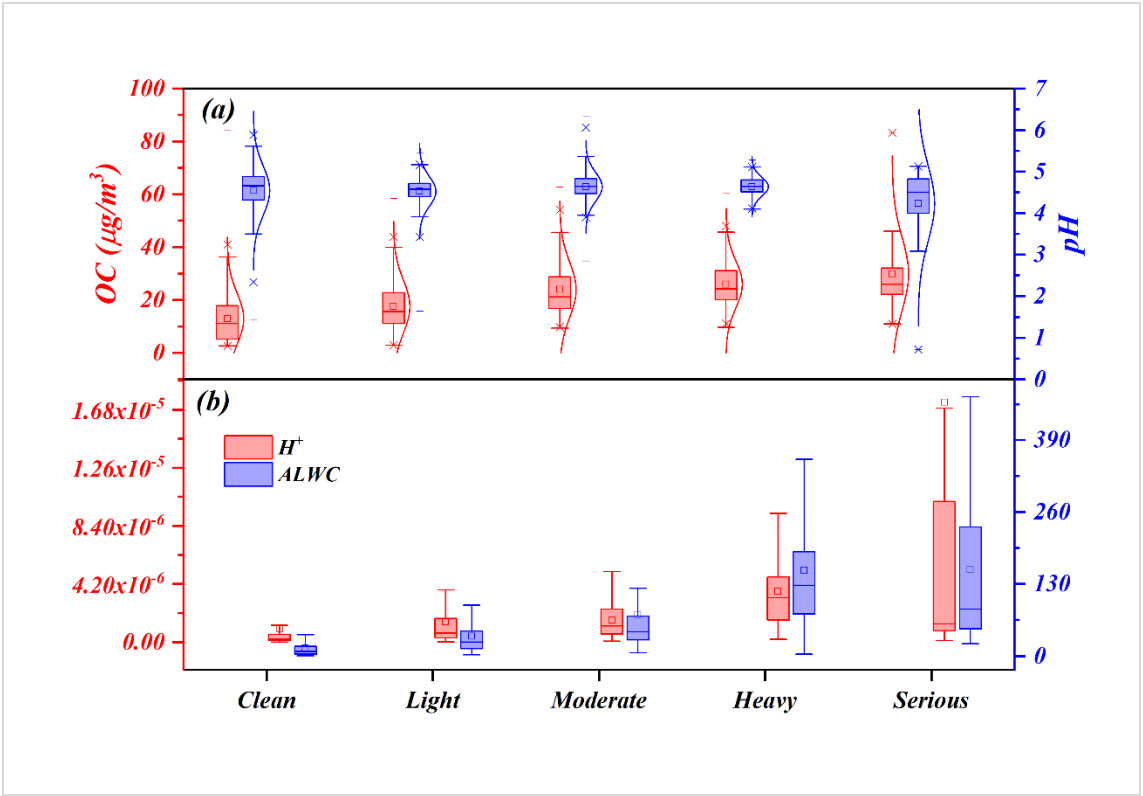

Fig. S14 Box-type of (a) OC and pH, (b) H^+ and ALWC corresponding to different pollution stages

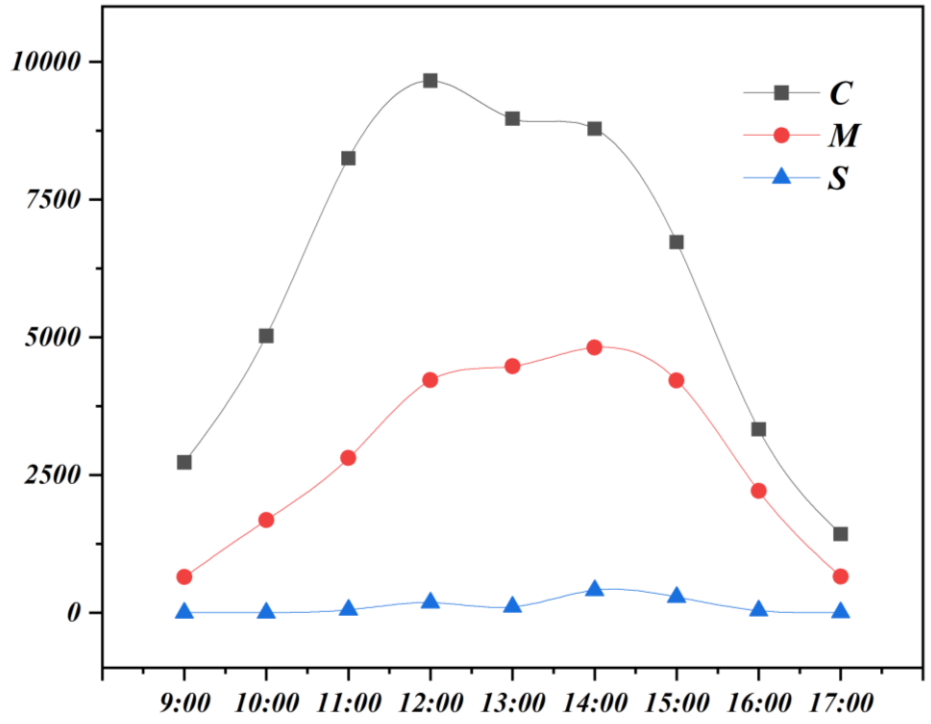

Fig. S15 Diurnal solar spectrophotometry at 380 nm at clean and moderate pollution stages

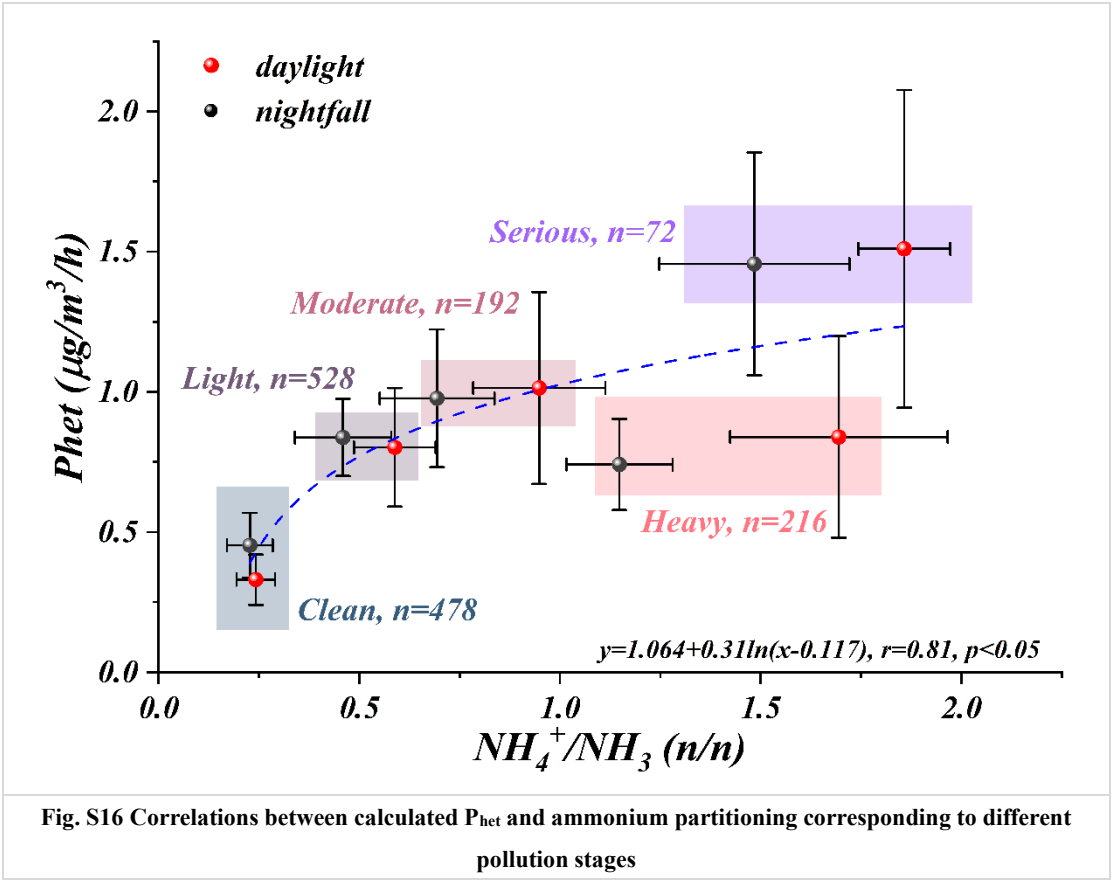

Fig. S16 Correlations between calculated P_{het} and ammonium partitioning corresponding to different pollution stages

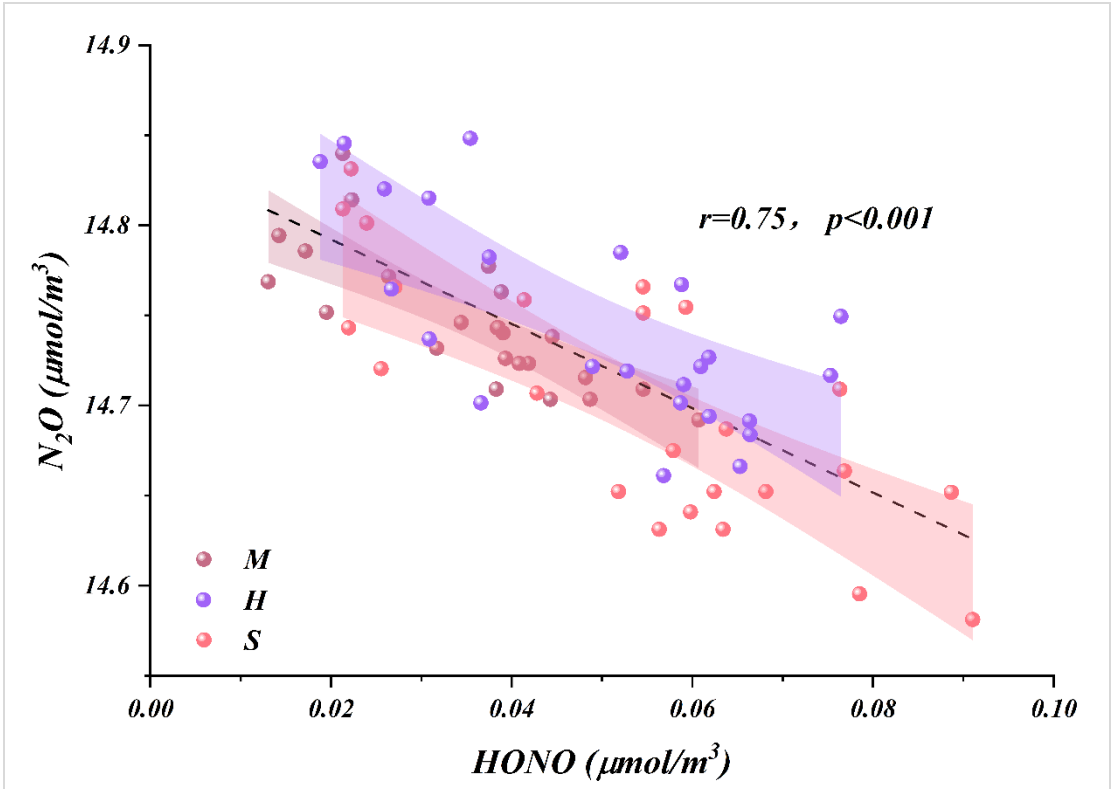

Fig. S17 Correlations between HONO and N_2O corresponding to pollution stages

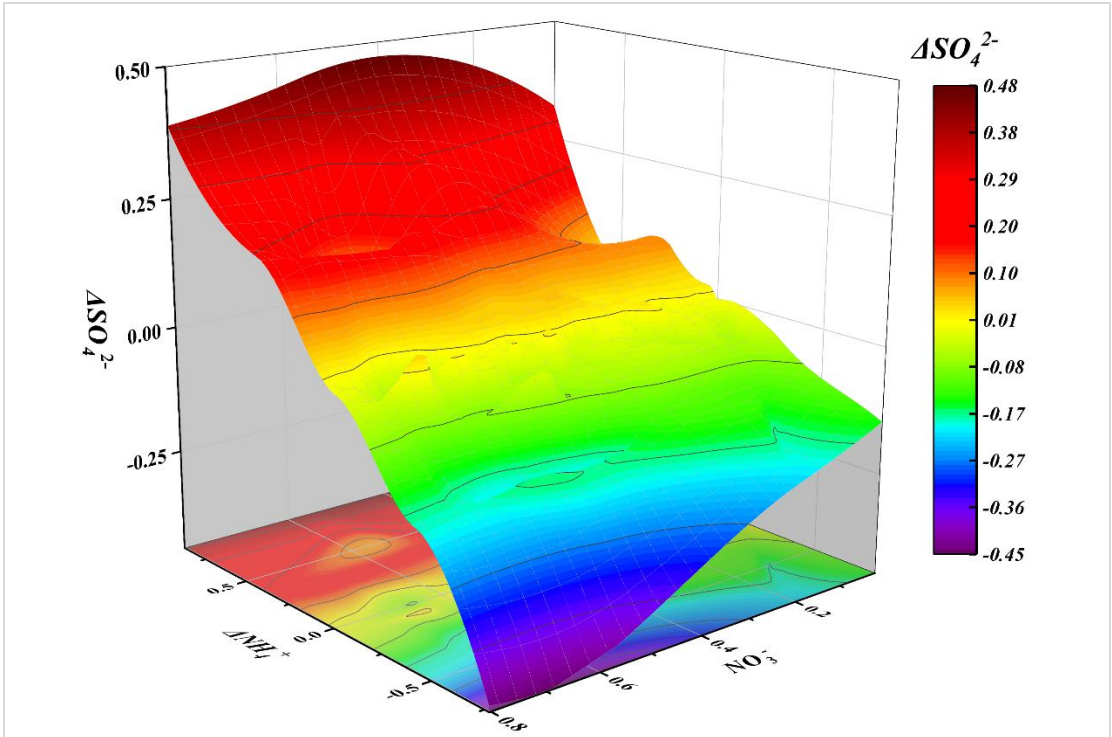

Fig. S18 Observation of inhibition and promotion of sulfate production by nitrate and ammonium, respectively. All data were matrixed to avoid interference caused by dimensionality

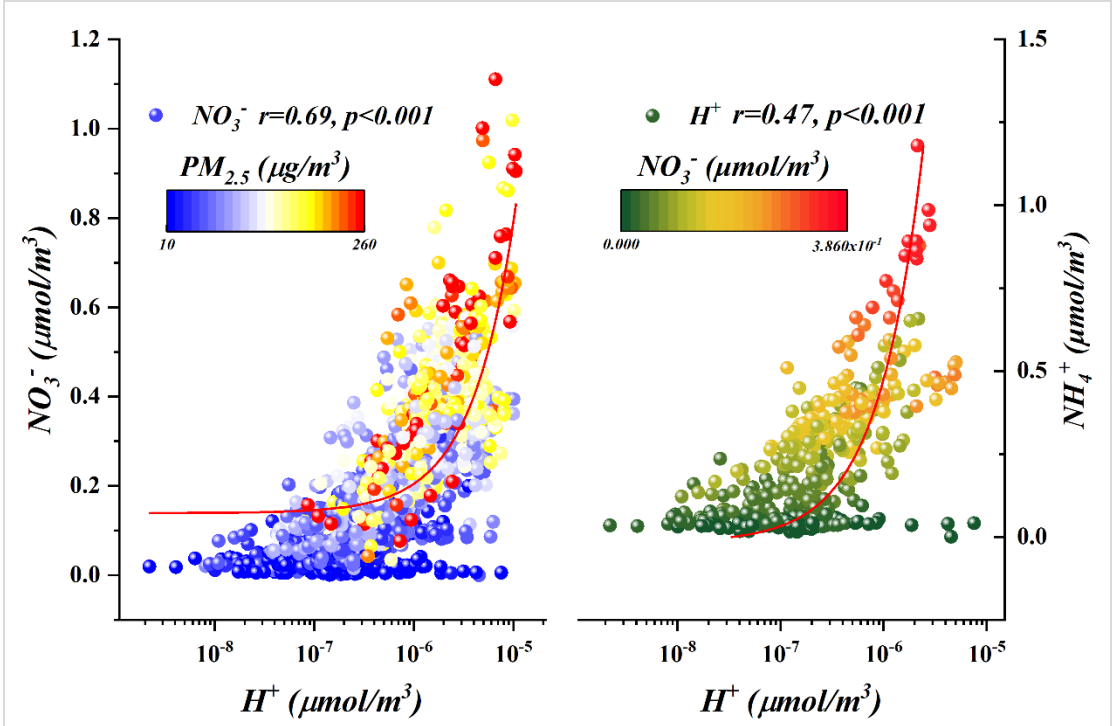

Fig. S19 Correlations between (a) H^+ and NO_3^- corresponding to $PM_{2.5}$ concentrations, (b) H^+ and NH_4^+ corresponding to NO_3^- molar concentrations

Table S1 Description of meteorological parameters and atmospheric pollutants

	Whole Campaign	*Clean*	*Light*	*Moderate*	*Heavy*	*Serious*
Temperature (°C)	-8.45±4.42	-7.92±5.0	-8.42±4.4	-7.73±4.0	-10.08±3.2	-9.13±3.3
RH (%)	65.59±14.1	59.48±15.0	64.64±11.7	68.33±12.5	77.27±10.3	71.13±11.9
Wind Speed (m/s)	1.43±0.87	1.79±1.2	1.25±0.6	1.07±0.5	1.01±0.5	1.15±0.47
Visibility (km)	37.50±20.4	52.36±18.1	38.12±14.1	30.77±20.3	15.01±10.0	18.98±11.7
Solar Radiation (w/m^2)	82.09±135.9	81.31±136.8	83.73±137.7	80.35±144.1	75.7±125.84	73.32±124.7
O_3 (μg/m^3)	43.41±27.4	45.29±26.5	38.79±22.9	54.23±35.3	38.71±24.3	30.94±14.3
NO_2 (μg/m^3)	44.56±18.6	35.72±19.8	45.18±16.4	47.40±14.8	51.99±17.6	57.10±21.1
NO_x (μg/m^3)	65.62±35.2	51.65±32.5	69.91±29.3	63.58±34.3	82.03±41.0	80.93±40.0
SO_2 (μg/m^3)	18.97±15.0	14.59±10.2	21.72±11.1	21.52±11.8	15.01±11.1	33.08±43.4
CO (mg/m^3)	1.57±0.75	1.06±0.66	1.58±0.6	1.82±0.6	2.18±0.6	2.40±0.8
NH_3 (μg/m^3)	5.55±4.07	5.08±3.84	5.24±3.96	6.31±4.43	6.37±3.37	6.42±6.09
PM_1 (μg/m^3)	63.18±96.0	32.02±23.2	55.27±25.4	86.16±143.9	90.47±27.7	170.7±316.7
$PM_{2.5}$ (μg/m^3)	84.75±84.5	39.11±31.1	71.21±35.9	112.38±144.6	150.10±46.0	192.14±162.9
PM_{10} (μg/m^3)	108.5±68.3	63.05±42.8	98.95±45.8	128.77±58.8	177.55±53.2	200.97±114.6
PM_1 /$PM_{2.5}$	0.84±0.39	0.87±0.08	0.92±0.06	0.94±0.02	0.95±0.02	0.96±0.01
$PM_{2.5}$ /PM_{10}	0.71±0.19	0.73±0.15	0.84±0.11	0.89±0.06	0.93±0.05	0.93±0.04
pH	4.54±0.51	4.54±0.59	4.52±0.35	4.63±0.34	4.64±0.22	4.16±1.26
ALWC (μg/m^3)	57.49±85.2	13.65±18.8	35.22±32.4	74.41±84.67	154.8±114.9	156.49±153

Notes: all datasets were presented as mean± S.D.

Table S2 Description of water-soluble ions with haze aggravation

	Clean	*Light*	*Moderate*	*Heavy*	*Serious*
Na^+ (μmol/m^3)	0.007±0.007	0.009±0.01	0.009±0.01	0.005±0.01	0.006±0.01
K^+ (μmol/m^3)	0.007±0.007	0.012±0.01	0.058±0.23	0.022±0.01	0.209±0.84
Mg^{2+} (μmol/m^3)	0.001±0.002	0.003±0.01	0.014±0.04	0.005±0.01	0.050±0.12
Ca^{2+} (μmol/m^3)	0.006±0.005	0.007±0.01	0.006±0.01	0.004±0.01	0.006±0.01
NH_4^+ (μmol/m^3)	0.235±0.21	0.518±0.31	0.810±0.38	1.399±0.54	1.572±0.62
NO_3^- (μmol/m^3)	0.094±0.09	0.226±0.12	0.321±0.12	0.461±0.18	0.548±0.32
SO_4^{2-} (μmol/m^3)	0.064±0.06	0.137±0.10	0.232±0.15	0.438±0.20	0.472±0.34
Cl^- (μmol/m^3)	0.051±0.04	0.058±0.04	0.105±0.23	0.093±0.04	0.234±0.74
Remained- NH_4^+ (μmol/m^3)	0.045±0.05	0.08650.087±	0.141±0.13	0.280±0.121	0.316±0.11

Note: Remained-ammonium = $[NH_4^+]$-1.5×$[SO_4^{2-}]$-$[NO_3^-]$

References:

Chang-Graham, A. L., Profeta, L. T. M., Johnson, T. J., Yokelson, R. J., Laskin, A., and Laskin, J.: Case Study of Water-Soluble Metal Containing Organic Constituents of Biomass Burning Aerosol, Environ. Sci. Technol., 45, 1257-1263, 10.1021/es103010j, 2011.

Clegg, S. L. and Brimblecombe, P.: Equilibrium partial pressures and mean activity and osmotic coefficients of 0-100% nitric acid as a function of temperature, The Journal of Physical Chemistry, 94, 5369-5380, 10.1021/j100376a038, 1990.

Cui, Y., Frie, A. L., Dingle, J. H., Zimmerman, S., Frausto-Vicencio, I., Hopkins, F., and Bahreini, R.: Influence of Ammonia and Relative Humidity on the Formation and Composition of Secondary Brown Carbon from Oxidation of 1-Methylnaphthalene and Longifolene, ACS Earth and Space Chem., 5, 858-869, 10.1021/acsearthspacechem.0c00353, 2021.

Gao, J., Wei, Y., Shi, G., Yu, H., Zhang, Z., Song, S., Wang, W., Liang, D., and Feng, Y.: Roles of RH, aerosol pH and sources in concentrations of secondary inorganic aerosols, during different pollution periods, Atmos. Environ., 241, 117770, https://doi.org/10.1016/j.atmosenv.2020.117770, 2020.

Guo, H., Liu, J., Froyd, K. D., Roberts, J. M., Veres, P. R., Hayes, P. L., Jimenez, J. L., Nenes, A., and Weber, R. J.: Fine particle pH and gas–particle phase partitioning of inorganic species in Pasadena, California, during the 2010 CalNex campaign, Atmos. Chem. Phys., 17, 5703-5719, 10.5194/acp-17-5703-2017, 2017.

Guo, H., Sullivan, A. P., Campuzano-Jost, P., Schroder, J. C., Lopez-Hilfiker, F. D., Dibb, J. E., Jimenez, J. L., Thornton, J. A., Brown, S. S., Nenes, A., and Weber, R. J.: Fine particle pH and the partitioning of nitric acid during winter in the northeastern United States, J. Geophys. Res. Atmos., 121, 10,355-310,376, https://doi.org/10.1002/2016JD025311, 2016.

Guo, H., Xu, L., Bougiatioti, A., Cerully, K. M., Capps, S. L., Hite Jr, J. R., Carlton, A. G., Lee, S. H., Bergin, M. H., Ng, N. L., Nenes, A., and Weber, R. J.: Fine-particle water and pH in the southeastern United States, Atmos. Chem. Phys., 15, 5211-5228, 10.5194/acp-15-5211-2015, 2015.

Hua, W., Chen, Z. M., Jie, C. Y., Kondo, Y., Hofzumahaus, A., Takegawa, N., Chang, C. C., Lu, K. D., Miyazaki, Y., Kita, K., Wang, H. L., Zhang, Y. H., and Hu, M.: Atmospheric hydrogen peroxide and organic hydroperoxides during PRIDE-PRD'06, China: their concentration, formation mechanism and contribution to secondary aerosols, Atmos. Chem. Phys., 8, 6755-6773, 10.5194/acp-8-6755-2008, 2008.

Huang, R.-J., Duan, J., Li, Y., Chen, Q., Chen, Y., Tang, M., Yang, L., Ni, H., Lin, C., Xu, W., Liu, Y., Chen, C., Yan, Z., Ovadnevaite, J., Ceburnis, D., Dusek, U., Cao, J., Hoffmann, T., and O'Dowd, C. D.: Effects of NH_3 and alkaline metals on the formation of particulate sulfate and nitrate in wintertime Beijing, Sci. Total Environ., 717, 137190, https://doi.org/10.1016/j.scitotenv.2020.137190, 2020.

Liu, Z., Xie, Y., Hu, B., Wen, T., Xin, J., Li, X., and Wang, Y.: Size-resolved aerosol water-soluble ions during the summer and winter seasons in Beijing: Formation mechanisms of secondary inorganic aerosols, Chemosphere, 183, 119-131, https://doi.org/10.1016/j.chemosphere.2017.05.095, 2017.

Mauldin Iii, R. L., Berndt, T., Sipilä, M., Paasonen, P., Petäjä, T., Kim, S., Kurtén, T., Stratmann, F., Kerminen, V. M., and Kulmala, M.: A new atmospherically relevant oxidant of sulphur dioxide, Nature, 488, 193-196, 10.1038/nature11278, 2012.

Nozière, B., Dziedzic, P., and Córdova, A.: Inorganic ammonium salts and carbonate salts are efficient catalysts for aldol condensation in atmospheric aerosols, Physical chemistry chemical physics : PCCP, 12, 3864-3872, 10.1039/b924443c, 2010.

Paulot, F., Ginoux, P., Cooke, W. F., Donner, L. J., Fan, S., Lin, M. Y., Mao, J., Naik, V., and Horowitz, L. W.: Sensitivity of nitrate aerosols to ammonia emissions and to nitrate chemistry: implications for present and future nitrate optical depth, Atmos. Chem. Phys., 16, 1459-1477, 10.5194/acp-16-1459-2016, 2016.

Shi, G., Xu, J., Shi, X., Liu, B., Bi, X., Xiao, Z., Chen, K., Wen, J., Dong, S., Tian, Y., Feng, Y., Yu, H., Song, S.,

Zhao, Q., Gao, J., and Russell, A. G.: Aerosol pH Dynamics During Haze Periods in an Urban Environment in China: Use of Detailed, Hourly, Speciated Observations to Study the Role of Ammonia Availability and Secondary Aerosol Formation and Urban Environment, J. Geophys. Res. Atmos., 124, 9730-9742, https://doi.org/10.1029/2018JD029976, 2019.

Wang, H., Wang, X., Zhou, H., Ma, H., Xie, F., Zhou, X., Fan, Q., Lü, C., and He, J.: Stoichiometric characteristics and economic implications of water-soluble ions in $PM_{2.5}$ from a resource-dependent city, Environ. Res., 193, 110522, https://doi.org/10.1016/j.envres.2020.110522, 2021.

Xu, L., Duan, F., He, K., Ma, Y., Zhu, L., Zheng, Y., Huang, T., Kimoto, T., Ma, T., Li, H., Ye, S., Yang, S., Sun, Z., and Xu, B.: Characteristics of the secondary water-soluble ions in a typical autumn haze in Beijing, Environ. Pollut., 227, 296-305, https://doi.org/10.1016/j.envpol.2017.04.076, 2017.

Zhang, Q., Ma, X., Tie, X., Huang, M., and Zhao, C.: Vertical distributions of aerosols under different weather conditions: Analysis of in-situ aircraft measurements in Beijing, China, Atmos. Environ., 43, 5526-5535, https://doi.org/10.1016/j.atmosenv.2009.05.037, 2009.

Zhang, Q., Quan, J., Tie, X., Li, X., Liu, Q., Gao, Y., and Zhao, D.: Effects of meteorology and secondary particle formation on visibility during heavy haze events in Beijing, China, Sci. Total Environ., 502, 578-584, https://doi.org/10.1016/j.scitotenv.2014.09.079, 2015.

Zheng, B., Zhang, Q., Zhang, Y., He, K., Wang, K., Zheng, G., Duan, F., Ma, Y., and Kimoto, T.: Heterogeneous chemistry: a mechanism missing in current models to explain secondary inorganic aerosol formation during the January 2013 haze episode in North China, Atmos. Chem. Phys., 15, 2031-2049, 2015.

Zhou, H., Lü, C., He, J., Gao, M., Zhao, B., Ren, L., Zhang, L., Fan, Q., Liu, T., He, Z., Dudagula, Zhou, B., Liu, H., and Zhang, Y.: Stoichiometry of water-soluble ions in $PM_{2.5}$: Application in source apportionment for a typical industrial city in semi-arid region, Northwest China, Atmos. Res., 204, 149-160, https://doi.org/10.1016/j.atmosres.2018.01.017, 2018.